

Electronic Supplementary Information: Macroscopic Defects upon Decomposition of CO₂ Clathrate Hydrate Crystals

Stefan Arzbacher,^{*a,d} Nima Rahmatian,^a Alexander Ostermann,^b Bernhard Massani,^c
Thomas Loerting,^d and Jörg Petrasch^a

^a *illwerke vkw Endowed Professorship for Energy Efficiency, Research Center Energy, Vorarlberg University of Applied Sciences, Hochschulstraße 1, Dornbirn 6850, Austria. Tel: +43 5572 792 3803; E-mail: energie@fhv.at.*

^b *Department of Mathematics, University of Innsbruck, Technikerstraße 13, Innsbruck 6020, Austria.*

^c *Institute for Condensed Matter and Complex Systems, University of Edinburgh, EH9 3JZ, Edinburgh, UK.*

^d *Institute of Physical Chemistry, University of Innsbruck, Innrain 52c, Innsbruck 6020, Austria.*

Details on microcomputed tomography (μ CT) settings, temperature and mass calibration, leakage, the non-uniform temperature field, and segmentation error are discussed in this document. Furthermore, additional results are presented to complement the findings in the main manuscript.

1 Tomographic Setup

All computed tomography scans were done using the commercially available microcomputed tomography system phoenix nanotom-m 180, built by GE Sensing & Inspection Technologies, Wunstorf, Germany.¹ Table S1 summarizes the parameters used in all full rotation scans.

Table S1 μ CT scan parameters used for this work

Parameter	Value
Tube Voltage	70 kV
Tube Current	350 μ A
Magnification	16.67
Voxel Edge Length	6 μ m
Timing	750 ms
Scan Duration	60 min
Average	3
No. of Images	1200

2 Temperature Calibration

The sample temperature T_{low} , used in the main manuscript, refers to the temperature at the bottom of the cell. It is derived from the read-out temperature T_{read} of the thermocouple (K-type, $d = 1$ mm) positioned in the center of the aluminum base using a calibration curve. The calibration curve is obtained from a thin ($d = 75 \mu\text{m}$), pre-calibrated, K-type thermocouple which is brought into good thermal contact with the bottom surface of the cell to measure T_{low} in calibration experiments. In the calibration runs the cell is cooled to the set point temperatures $T_{\text{read}} \in \{203 \text{ K}, 213 \text{ K}, \dots, 293 \text{ K}\}$. One quick test scan (full rotation within 30 min) is done at each temperature while T_{low} is monitored. This procedure yields both an offset between T_{read} and T_{low} as well as small fluctuations in T_{low} due to asymmetric cool-

ing. Particularly, for $T_{\text{read}} < 243 \text{ K}$, where cooling with cold gaseous nitrogen ($\text{N}_2(\text{g})$) is necessary, deviations from cylindrical symmetry become visible. The result of the calibration measurement is shown in Figure S1. A quadratic function is eventually used to map T_{read} to T_{low} with an accuracy better than 1 K over the whole range of temperatures investigated. For $T_{\text{read}} > 243 \text{ K}$ the accuracy is even better than 0.2 K.

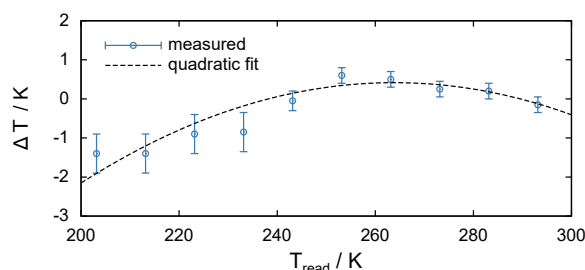


Fig. S1 Difference of read-out and cell bottom temperature ($\Delta T = T_{\text{read}} - T_{\text{low}}$) as a function of read-out temperature. Points with markers represent the difference as obtained from the calibration experiment. Error bars are derived from variations of ΔT during the calibration experiment. They are significantly larger for $T_{\text{read}} < 243 \text{ K}$ due to fluctuations caused by cooling with cold gaseous nitrogen. A quadratic function (dashed line) is used to map T_{read} to T_{low} .

3 Temperature Field

The unique design of our setup includes a non-uniform temperature field in the cell as well as the sample. Both, numerical simulations and experiments are used to determine the temperature distribution inside the cell as a function of cell bottom temperature T_{low} . The open source 3D solver ELMER² is used to solve the steady state heat conduction equation. Due to the small Grasshof number of the problem, convection inside the cell is neglected. In all simulations convective heat transfer to the environment is used (heat transfer coefficient $h = 25 \text{ W m}^{-2} \text{ K}^{-1}$, ambient temperature 298 K) while a fixed temperature boundary condition at the cell bottom is applied. Simulations are done for cell bottom temperatures $T_{\text{low}} \in \{173 \text{ K}, 183 \text{ K}, \dots, 293 \text{ K}\}$. In experiments done for the determination of the temperature

field the pre-calibrated thin thermocouple ($d = 75\mu\text{m}$) is positioned 3 mm above the bottom of the cell. It is then used to determine the temperature gradient close to the cell bottom. For that purpose the cell bottom temperature T_{low} is set to 13 different temperatures in the range from 184 K to 293 K and compared to the temperature of the thin thermocouple once stabilized. Figure S2 shows the results of the simulations and the temperature gradient measurements. Simulation results show that the temperature gradient is almost uniform and aligned along the cylindrical cell axis. Temperature gradient strengths are significant, particularly at low temperatures. The gradient strengths obtained from simulations underestimate the actual values because of the idealistic boundary conditions. At the same time, the measured values overestimate the gradient strength because the metallic thermocouple constitutes a heat bridge to the warm environment. Hence, a realistic estimation of the temperature gradient is found between the measured and simulated values.

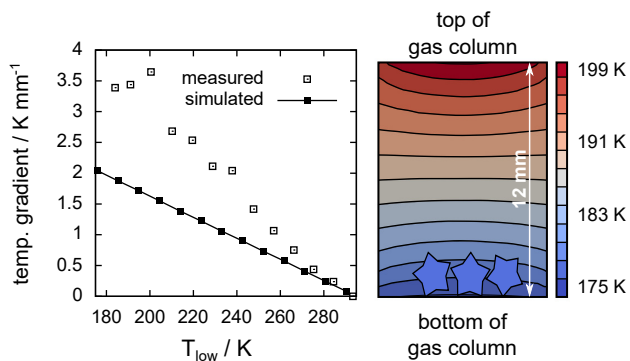


Fig. S2 Magnitude of temperature gradient inside the cell as a function of cell bottom temperature T_{low} (left) obtained from measurements and computer simulations. The result of a simulation (right) shows axial layers of uniform temperature and almost identical thickness indicating an almost uniform temperature gradient aligned along the cell axis.

The presence of a sample in the cell can have a significant impact on the temperature field. Thus, experiments and simulations with an empty cell provide only a rough estimate of the variation of temperature across the sample. While, at equilibrium conditions, the sample temperature at the coldest position (i.e., at the bottom of the cell) can be reliably determined using T_{low} , determination of the temperature at the warmest position (T_{high}) needs additional information. In our work, the vapor-ice-hydrate (V-I-H) equilibrium curve is used as an additional source of information. In closed system experiments, where hydrate is initially at sub-stable pressure, a settling of pressure implies either that there is no hydrate left or that the thermodynamic conditions reached the stability region. In the second case the settled experimental pressure has to be equal to the thermodynamic equilibrium pressure p_{equ} at the tempera-

ture T_{high} . Here, the software CSMGem³ is used to compute the thermodynamic equilibrium temperature (i.e., T_{high}) as a function of the settled experimental pressure interpreted as p_{equ} .

When the non-uniform temperature field changes over time, e.g. in case of heating, additional effects have to be considered. Figure S3(a) shows one possible pathway of a sample during the raise of the cell bottom temperature from $T_{\text{low},1}$ to $T_{\text{low},2}$. Since $T_{\text{high},1} > T_{\text{low},2}$ the inequality $p_{\text{equ.}}(T_{\text{high},1}) > p_{\text{equ.}}(T_{\text{low},2})$ holds. This implies that, no matter the exact pathway, the cold region of the sample remains in the hydrate stability region during the course of heating. Thus, in this case only the warmer regions of the sample decompose. In Fig. S3(b) a similar situation is shown for $T_{\text{low},2} > T_{\text{high},1}$. Here, also the cold region of the sample can decompose upon heating.

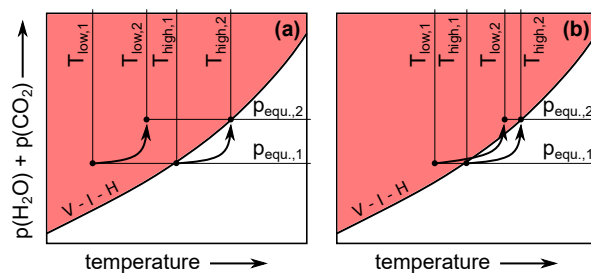


Fig. S3 Schematic of temperature change in a closed system at non-uniform temperature. T_{low} and T_{high} refer to the sample temperature at the coldest and warmest position in the cell, respectively. Subscripts 1 and 2 denote the start and the end of a heating process. Pressures $p_{\text{equ.,1}}$ and $p_{\text{equ.,2}}$ correspond to V-I-H equilibrium pressures at temperatures $T_{\text{high},1}$ and $T_{\text{high},2}$, respectively.

4 Leakage

Several pressure tests were done with N_2 and CO_2 gas in the absence of sample material. A leak rate of less than $1.6 \text{ mbarbar}^{-1} \text{ h}^{-1}$ is observed in five independent tests for CO_2 . In two pressure tests done with N_2 the leak rate is less than $0.3 \text{ mbarbar}^{-1} \text{ h}^{-1}$. This means that at a cell gauge pressure of 5 bar the reduction in pressure because of leakage is less than 1.5 mbar per hour for N_2 and less than 8 mbar per hour for CO_2 . This is comparable to the accuracy of the pressure sensor ($<6 \text{ mbar}$). Furthermore, even in the case of the roughly 50h long isothermal experiment at 253 K the relative error in gas mass because of leakage is estimated to be less than 3%. The difference in leak rate between CO_2 and N_2 can be explained with the generally higher permeation coefficient of CO_2 across the O-ring material (FKM, Viton).⁴ Note that small variations from the leak rates given here are possible in experiments since every new compression of the O-ring might change the overall permeation. Altogether, in our study the cell is treated as a closed system and gas loss due to leakage is neglected.

5 Mass Calibration

In our setup gas mass released by the hydrate is measured using the pressure signal only. A model, mapping pressure to released gas mass is derived here. Similar to our previous derivation⁵ we start off with the modified ideal gas law

$$pf(\Theta) = ZmR, \quad (\text{S1})$$

where

$$f(\Theta) = \int_V \frac{1}{\Theta(\mathbf{x})} dV \quad (\text{S2})$$

is a function of the temperature field $\Theta(\mathbf{x})$ in the cell. p is the absolute pressure of the cell gas with mass m , R is the specific gas constant, and Z is the compressibility factor, assumed to be constant for the temperatures and pressures considered. The combination of Eq. S1 and Dalton's law for the two-component gas N_2 and CO_2 yields

$$\begin{aligned} pf(\Theta) &= (p_{\text{N}_2} + p_{\text{CO}_2})f(\Theta) \\ &= p_{\text{N}_2}f(\Theta) + p_{\text{CO}_2}f(\Theta) \\ &= (ZmR)_{\text{N}_2} + (ZmR)_{\text{CO}_2}, \end{aligned} \quad (\text{S3})$$

where p is the total (absolute) pressure accessible in our measurements. Quantities with subscript CO_2 and N_2 refer to the two individual components of the gas. Note that water is neglected as a third component due to its comparably small partial pressure.

In experiments where the cell remains closed and leakage is neglected the time dependence of the total pressure is described by

$$p(t)f(\Theta(t)) = (ZmR)_{\text{N}_2} + (Zm(t)R)_{\text{CO}_2}. \quad (\text{S4})$$

Rearranging yields the guest mass as a function of time:

$$m_{\text{CO}_2}(t) = \frac{p(t)f(\Theta(t)) - (ZmR)_{\text{N}_2}}{Z_{\text{CO}_2}R_{\text{CO}_2}}. \quad (\text{S5})$$

Since $p(t)$ is precisely measured $m_{\text{CO}_2}(t)$ can be evaluated given the knowledge of $f(\Theta)$ and the initial mass of nitrogen (m_{N_2}), which can be easily derived from the initial conditions of the experiment ($m_{\text{CO}_2}(t=0) = 0$). Note that this derivation is only valid in the quasi-stationary case where $\dot{\Theta}(t) \approx 0$. In every other case deviations from this model caused by thermodynamic non-equilibrium have to be considered. Hence, gas mass data obtained from this model equation during periods of heating or cooling are not reliable.

The only task left now is the determination of $f(\Theta)$ or $g(\Theta) := f(\Theta)^{-1}$. This task is equivalent to the determination of thermal gas expansion or contraction. Fortunately, this is feasible using careful calibration experiments with a cell filled with gas only. Figure S4 shows

the results of such experiments done using air, CO_2 , and Ar (Ar is used for a set of independent experiments not part of this work). In seven out of eight runs T_{low} is raised by 1 K min^{-1} from 210 K to 283 K. In one experiment (labelled "no ramp") equilibrated temperature fields are used in order to estimate the effect of a transient temperature field. There, long waiting periods at nine different temperature conditions allow the temperature field to relax. No significant deviation between results obtained from the transient and the steady temperature field experiment is observed. However, the ambient temperature T_{amb} in the μCT cabin differed between the experiments and affected the thermal expansion.

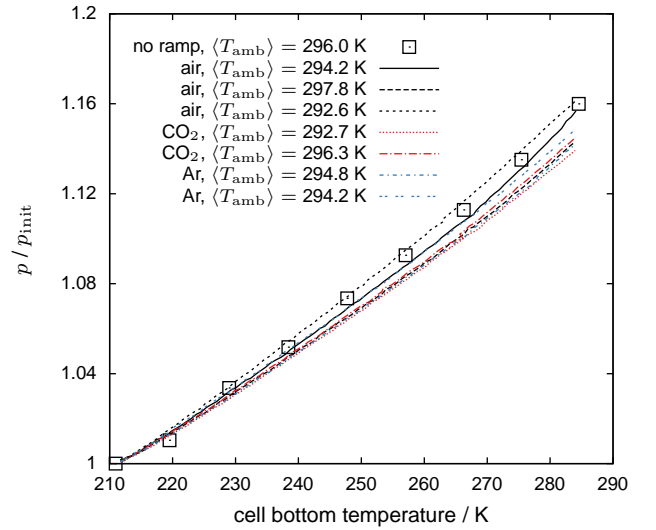


Fig. S4 Thermally induced gas expansion obtained from temperature ramping experiments (ramp rate of 1 K/min with respect to T_{low}) with air, CO_2 , and Ar. In addition, the gas expansion of air in equilibrated temperature fields (box markers) is provided for nine different temperature conditions. Gas expansion is generally expressed as the ratio of absolute pressure p to absolute pressure p_{init} at the beginning of the experiment. $\langle T_{\text{amb}} \rangle$ denotes the mean ambient temperature over the course of the temperature ramping experiment.

An assumption in the derivation of the thermal expansion model is that $g(\Theta)$ can be approximated using a function $\tilde{g}(T_{\text{low}}, T_{\text{amb}})$ with the two temperatures T_{low} and T_{amb} as arguments. We set

$$g(\Theta) \approx \tilde{g}(T_{\text{low}}, T_{\text{amb}}) = \left[a + b \left(\frac{T_{\text{low}}}{T_{\text{amb}}} \right) + c \left(\frac{T_{\text{low}}}{T_{\text{amb}}} \right)^2 \right] \cdot \frac{T_{\text{amb}}}{(a + b + c)V} \quad (\text{S6})$$

with fit parameters a , b , c , and the cell volume V . Note that, without loss of generality, the parameter a can be fixed at any value different from zero. In a uniform temperature field with $T_{\text{low}} = T_{\text{amb}}$ the condition $\tilde{g}(T_{\text{amb}}, T_{\text{amb}}) = g(T_{\text{amb}}) = f(T_{\text{amb}})^{-1} = T_{\text{amb}}/V$ holds automatically. Hence, the fitting model complies with the ideal gas law, regardless of the choice of parameters. Af-

ter fixing $a := 1.0$ the fit parameters b and c are determined using the relation $p(t)f(\Theta(t)) = \text{const.}$, i.e.,

$$\frac{p}{p_{\text{init}}} = \frac{\tilde{g}(T_{\text{low}}, T_{\text{amb}})}{\tilde{g}(T_{\text{low,init}}, T_{\text{amb,init}})} \quad (\text{S7})$$

for each of the seven measured pressure ratio curves shown in Fig. S4. This leads to the sets $\{b_i\}_{i=1}^7$ and $\{c_i\}_{i=1}^7$ of fit parameters with corresponding standard deviations $\{\sigma_{b,i}\}_{i=1}^7$ and $\{\sigma_{c,i}\}_{i=1}^7$. A weighted arithmetic mean (e.g. $b = \frac{1}{M} \sum b_i \sigma_{b,i}^{-1}$ with $M = \sum \sigma_{b,i}^{-1}$, etc.) is computed for each parameter set and used in the final model function for thermal expansion. This eventually yields the model parameters $b = -0.2187$ and $c = 0.5220$.

Figure S5 shows the relative error of the model for thermal expansion derived above. The error is less than 1.5% over the full temperature range investigated and independent of the choice of gas. This relative error translates directly to the relative error in the determination of released gas mass.

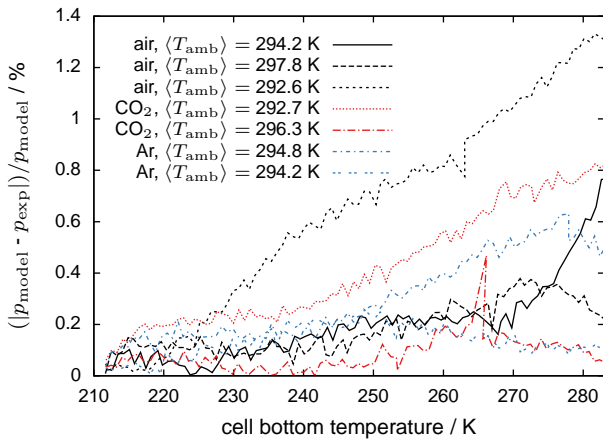


Fig. S5 Relative error of the thermal gas expansion model. The model is used to predict the thermally induced gas expansion based on cell bottom temperature T_{low} and cell ambient temperature T_{amb} only. Modelled absolute pressures p_{model} are compared with measured pressures p_{exp} obtained from the temperature ramping experiments (ramp rate 1 K/min with respect to T_{low}) with air, CO_2 , and Ar.

6 Image Processing

Reconstruction of the radiograms with GE's phoenix datos|x reconstruction software (GE Sensing & Inspection Technologies, Germany) yields raw three dimensional raster image data with a gray scale resolution of 16 bit and a voxel edge length of $6\mu\text{m}$ (cf. Fig. S6(a)). The raw images contain a noticeable level of noise which would complicate image segmentation. The application of a simple three dimensional median filter with a kernel size of 7 voxel reduces the noise level but preserves small features and edges (cf. Fig. S6(b)). After filtering, the raster image data is compressed to 8 bit gray scale values and scaled to $12\mu\text{m}$ voxel edge length using the software VG Studio MAX 2.2 (Volume Graphics GmbH,

Germany). This reduces the file size of the image stack for subsequent segmentation, done with our own three-dimensional implementation⁵ of the random walk algorithm of Grady.⁶ Figure S6(c) shows the phases air, hydrate, and decomposed hydrate in a slice across the segmented sample. Note that all visual inspection of the image data is done using the 16 bit ($6\mu\text{m}$ voxel edge length) data set. Segmented images ($12\mu\text{m}$ voxel edge length) are solely used for the determination of phase volumes. For that purpose a reduction of resolution from $6\mu\text{m}$ to $12\mu\text{m}$ voxel edge length is found to be insignificant.

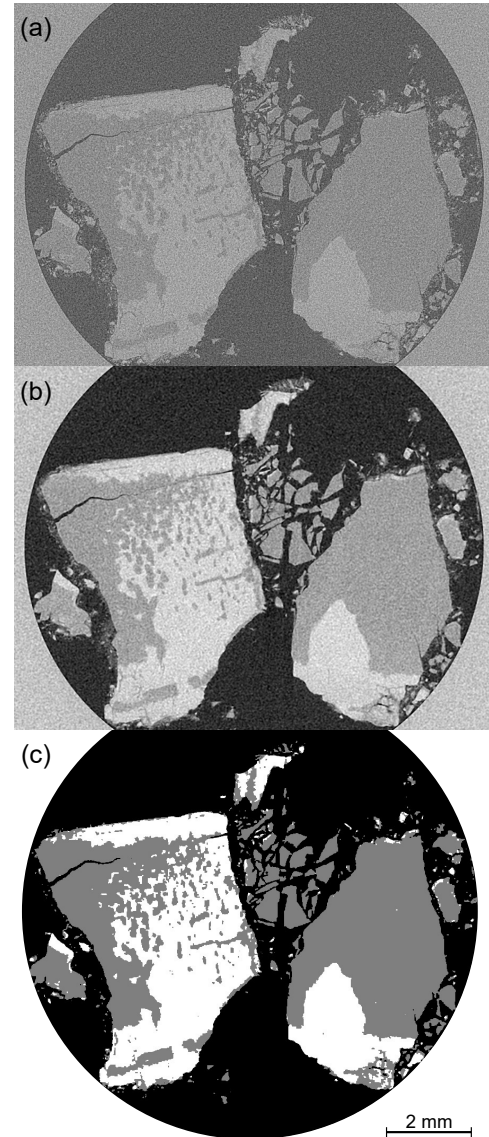


Fig. S6 Image processing procedure illustrated for one tomogram. (a) Original tomogram. (b) Tomogram after denoising using a median filter with a kernel size of 7 pixels. (c) Image after phase segmentation into hydrate (white), decomposed hydrate (gray), and gas (black).

After segmentation, voxel counting is used for the determination of the volumes of individual phases. An estimation of segmentation error (i.e., the difference between the volumes determined by voxel counting and the actual volumes of the phases) is difficult when based

on image data alone. The availability of additional volume related information in form of the released gas mass data alleviates this problem. Figure S7 shows the relation of the volume of decomposed hydrate (determined by voxel counting) and the released gas mass for the three experiments described in the main manuscript. In

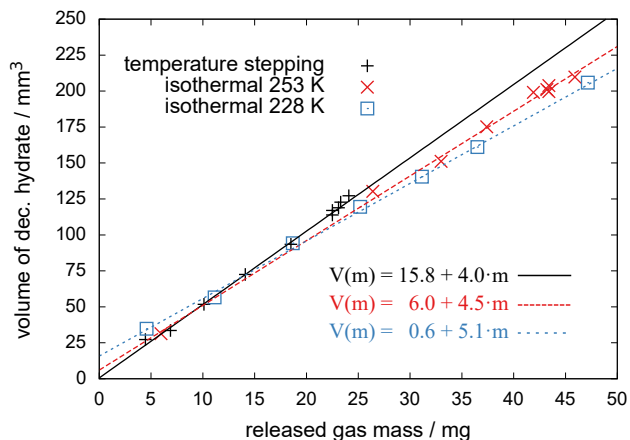


Fig. S7 Relation between volume of decomposed hydrate and released gas mass as obtained from the experiments described in the main manuscripts.

all three cases the data points obtained from the experiment can be approximated using $V(m) = V_0 + v \cdot m$. Physically, V_0 refers to the volume of hydrate which is already decomposed before the experiment is started, meaning before gas release can be detected. Table S2 lists values of V_0 and v and corresponding uncertainties. All data points deviate from their linear fit curves by less than 4 mm^3 .

Table S2 Parameters of the fitting function $V(m) = V_0 + v \cdot m$ and corresponding uncertainties

Experiment	V_0 (mm^3)	v ($\text{mm}^3 \text{mg}^{-1}$)
Temp. Stepping	0.6 ± 1.9	5.1 ± 0.11
Isothermal 228 K	15.8 ± 2.7	4.0 ± 0.11
Isothermal 253 K	6.0 ± 3.5	4.5 ± 0.09

7 Additional Results

Figures S8–S10 show three-dimensional illustrations of decomposing hydrates measured in the experiments described in the main manuscript. Pressure and temperature data of an isothermal experiment showing an intense degree of self-preservation are depicted in Fig. S11.

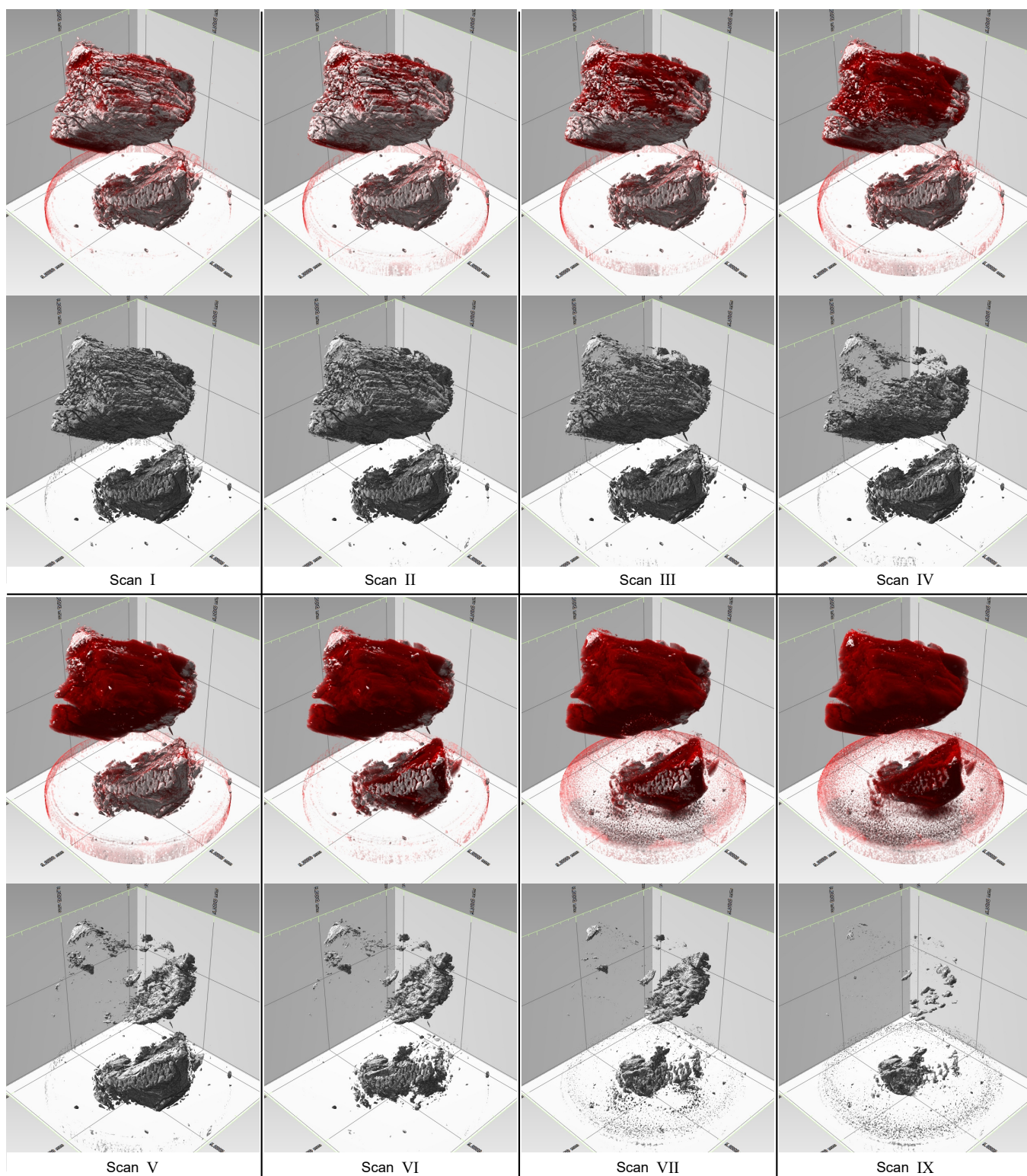


Fig. S8 3D illustration of decomposing hydrate at eight different stages of decomposition. The views are obtained from tomograms collected during the temperature stepping experiment. Roman numerals refer to the scan numbers as labeled in Fig. 5 of the main manuscript. The views are given in top-bottom pairs. The top view always shows both hydrate (gray) and decomposed hydrate (red). The bottom view shows hydrate only. The ice particles which were part of this experiment are removed from the views in post processing.

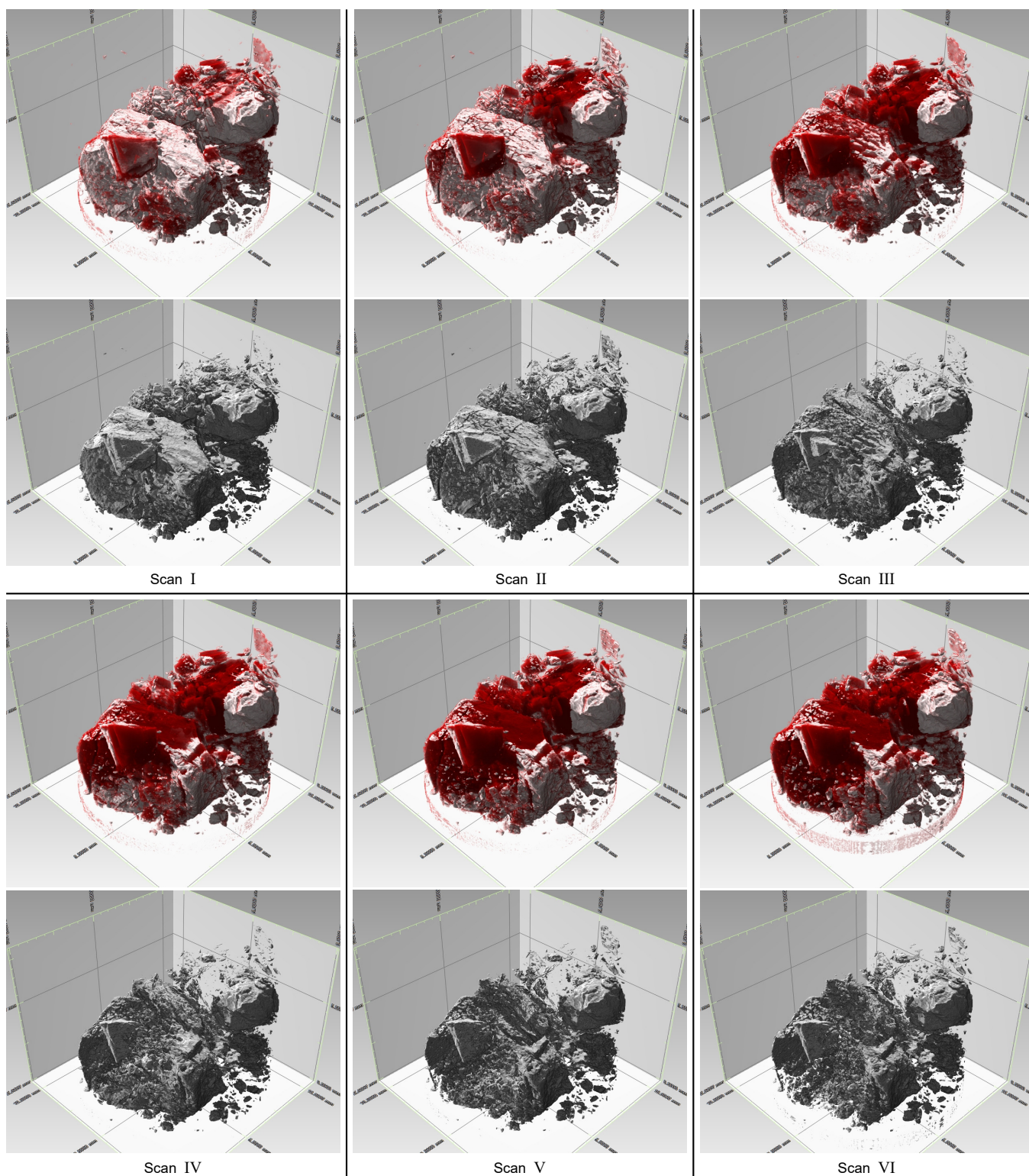


Fig. S9 3D illustration of decomposing hydrate at six different stages of decomposition. The views are obtained from tomograms collected during the isothermal experiment at 228 K. Roman numerals refer to the scan numbers as labeled in Fig. 10 of the main manuscript. The views are given in top-bottom pairs. The top view always shows both hydrate (gray) and decomposed hydrate (red). The bottom view shows hydrate only.

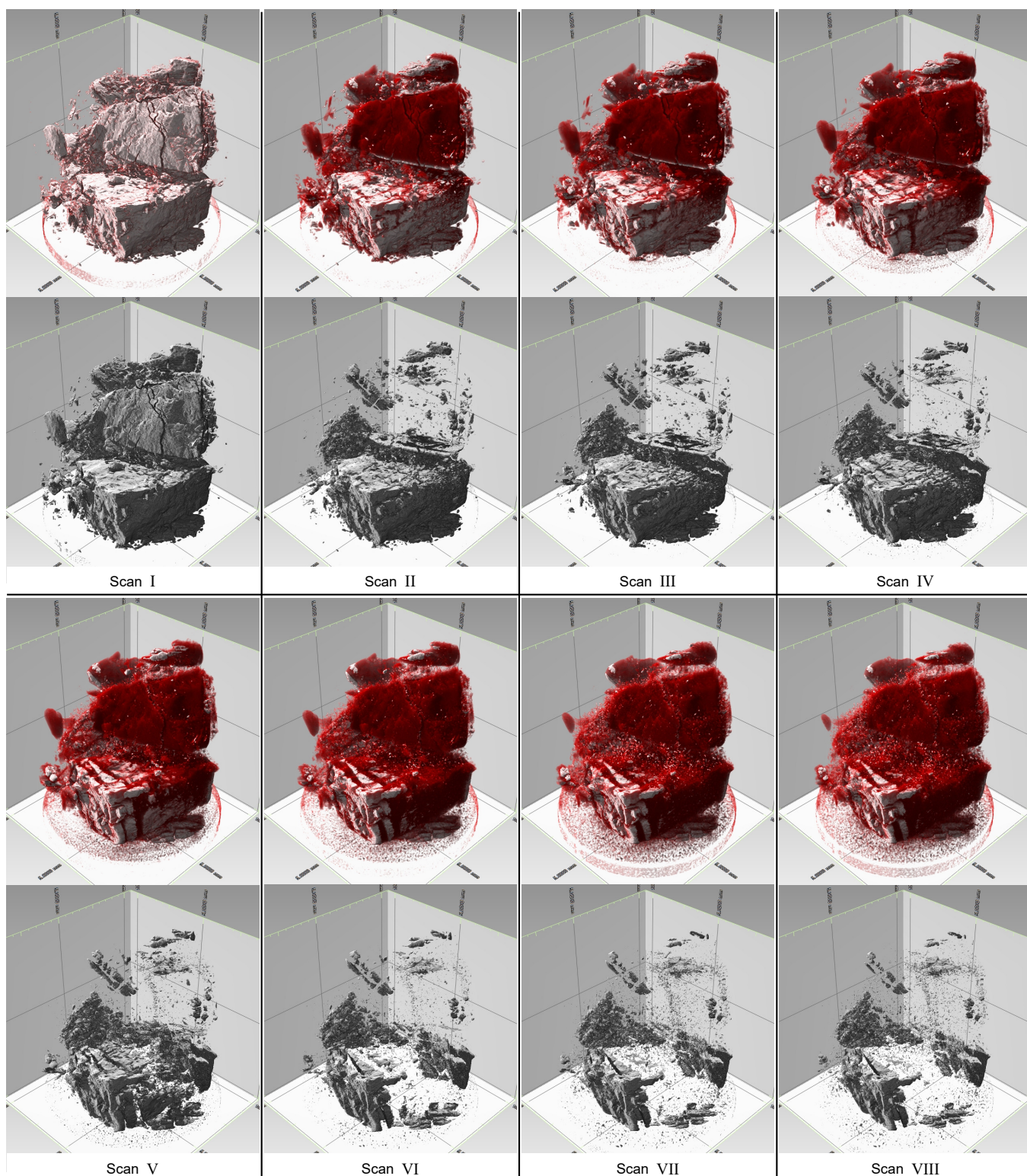


Fig. S10 3D illustration of decomposing hydrate at eight different stages of decomposition. The views are obtained from tomograms collected during the isothermal experiment at 253 K. Roman numerals refer to the scan numbers as labeled in Fig. 10 of the main manuscript. The views are given in top-bottom pairs. The top view always shows both hydrate (gray) and decomposed hydrate (red). The bottom view shows hydrate only.

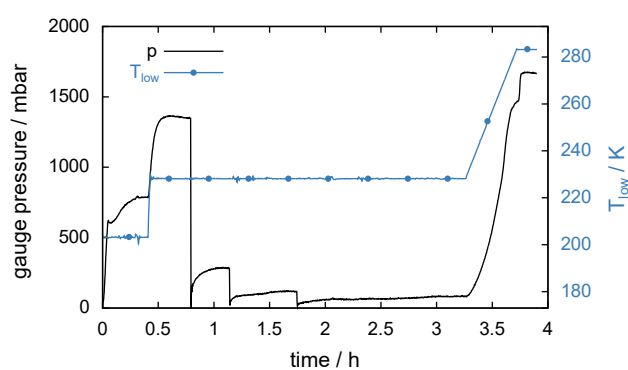


Fig. S11 Pressure and temperature as a function of time obtained from an isothermal experiment at 228 K with a $\text{CO}_2 \cdot 30\text{H}_2\text{O}$ hydrate sample. The rate of hydrate dissociation is very small after the first depressurization at 1 h experiment time. After the second depressurization event hydrate dissociation seems to stop almost completely. The pressure release at the end of the experiment shows that approximately 50% of the hydrate remained outside the stability region at 228 K for roughly 2 h showing almost no release of gas at all. The jump in pressure at 3.7 h experiment time (corresponding to $T_{low} = 283\text{ K}$) implies that approximately 5% of the hydrate outlasted even the onset of melting. This is probably due to the temperature depression caused by the melting of the large amount of ice contained in the sample.

References

- 1 O. Brunke, E. Neuser, A. Suppes and S. Chandgdar, *The e-Journal of Nondestructive Testing*, 2014, **20**, 1–9.
- 2 P. Råbak, M. Malinen, J. Ruokolainen, A. Pursula and T. Zwinger, *Elmer Models Manual*, CSC–IT Cent. Sci. Hels. Finl., 2013.
- 3 E. D. Sloan and C. A. Koh, *Clathrate Hydrates of Natural Gases*, CRC Press, Boca Raton, FL, 3rd edn, 2007.
- 4 P. Sturm, M. Leuenberger, C. Sirignano, R. E. M. Neubert, H. A. J. Meijer, R. Langenfelds, W. A. Brand and Y. Tohjima, *J. Geophys. Res. Atmospheres*, 2004, **109**, D04309.
- 5 S. Arzbacher, J. Petrasch, A. Ostermann and T. Loerting, *Materials*, 2016, **9**, 668.
- 6 L. Grady, *IEEE Trans. Pattern Anal. Mach. Intell.*, 2006, **28**, 1768–1783.